RESEARCH ARTICLE

CARBON ENERGY WILEY

Electrochemical evolution of a metal oxyhydroxide surface on two-dimensional layered metal phosphorus trisulfides enables the oxidation of amine to nitrile

Binglan Wu[1,2,3,4] | Karim Harrath[5] | Marshet Getaye Sendeku[2,6] |
Tofik Ahmed Shifa[7] | Yuxin Huang[1] | Jing Tai[8] | Fekadu Tsegaye Dajan[2] |
Kassa Belay Ibrahim[7] | Xueying Zhan[2] | Zhenxing Wang[2] | Elisa Moretti[7] |
Ying Yang[3] (ID) | Fengmei Wang[1,2] | Alberto Vomiero[7,9] (ID)

[1]State Key Laboratory of Chemical Resource Engineering, College of Chemistry, Beijing University of Chemical Technology, Beijing, China

[2]CAS Key Laboratory of Nanosystem and Hierarchical Fabrication, National Center for Nanoscience and Technology (NCNST), Beijing, China

[3]Shaanxi Provincial Key Laboratory of Electroanalytical Chemistry, Key Laboratory of Synthetic and Natural Functional Molecule of the Ministry of Education, College of Chemistry & Materials Science, Northwest University, Xi'an, China

[4]State Key Laboratory of Multiphase Flow in Power Engineering, International Research Center for Renewable Energy, Xi'an Jiaotong University, Shaanxi, China

[5]Fundamental Science Center of Rare Earths, Ganjiang Innovation Academy, Chinese Academy of Science, Ganzhou, China

[6]Ocean Hydrogen Energy R&D Center, Research Institute of Tsinghua University in Shenzhen, Shenzhen, China

[7]Department of Molecular Sciences and Nanosystems, Ca' Foscari University of Venice, Venezia Mestre, Italy

[8]Testing and Analysis Center, Institute of Chemistry Chinese Academy of Sciences, Beijing, China

[9]Department of Engineering Sciences and Mathematics, Division of Materials Science, Luleå University of Technology, Luleå, Sweden

Correspondence
Alberto Vomiero and Elisa Moretti,
Department of Molecular Sciences and
Nanosystems, Ca' Foscari University of
Venice, Via Torino 155, 30172 Venezia
Mestre, Italy.
Email: alberto.vomiero@ltu.se and
elisa.moretti@unive.it

Ying Yang, Shaanxi Provincial Key
Laboratory of Electroanalytical Chemistry,
Key Laboratory of Synthetic and Natural
Functional Molecule of the Ministry of
Education, College of Chemistry &
Materials Science, Northwest University,
Xi'an 710127, China.
Email: yingyang@nwu.edu.cn

Fengmei Wang, State Key Laboratory of
Chemical Resource Engineering, College
of Chemistry, Beijing University of

Abstract

Selective oxidation of amines to imines through electrocatalysis is an attractive and efficient way for the chemical industry to produce nitrile compounds, but it is limited by the difficulty of designing efficient catalysts and lack of understanding the mechanism of catalysis. Herein, we demonstrate a novel strategy by generation of oxyhydroxide layers on two-dimensional iron-doped layered nickel phosphorus trisulfides ($Ni_{1-x}Fe_xPS_3$) during the oxidation of benzylamine (BA). In-depth structural and surface chemical characterizations during the electrocatalytic process combined with theoretical calculations reveal that $Ni_{(1-x)}Fe_xPS_3$ undergoes surface reconstruction under alkaline conditions to form the metal oxyhydroxide/phosphorus trichalcogenide ($NiFeOOH/Ni_{1-x}Fe_xPS_3$) heterostructure. Interestingly, the generated hetero-interface facilitates BA oxidation with a low onset potential of 1.39 V and Faradaic efficiency of 53% for benzonitrile (BN) synthesis. Theoretical

Binglan Wu, Karim Harrath, and Marshet Getaye Sendeku contributed equally to this study.

Chemical Technology, Beijing 100029, China.
Email: wangfm@buct.edu.cn

calculations further indicate that the as-formed $NiFeOOH/Ni_{1-x}Fe_xPS_3$ heterostructure could offer optimum free energy for BA adsorption and BN desorption, resulting in promising BN synthesis.

KEYWORDS

2D layered materials, benzylamine oxidation, metal phosphorus trichalcogenides, surface-reconstructed heterostructure

1 | INTRODUCTION

Electrocatalysis stands out as a sustainable and environmentally friendly technology, enabling the synthesis of diverse high-value chemicals at ambient temperature and pressure.[1-3] Of particular interest is the synthesis of nitriles from amines via an oxidation reaction, which stems from their importance in the production of synthetic fibers and plastics, pharmaceuticals, textiles, herbicides, and agrochemicals.[4-6] The conventional methods for synthesizing nitrile compounds often rely on the use of hazardous cyanide reagents, including vanadium or chromium cyanides, which entail significant environmental risks.[7-10] In contrast, the electrocatalytic oxidation of primary amines, like benzylamine (BA), can lead to conversion into benzonitrile (BN) by electrocatalytic dehydrogenation under mild conditions without utilizing strong oxidants. Furthermore, the miscibility of BA[11] with water could offer a promising platform to realize BN synthesis at the anode in an aqueous electrolyte to couple with green hydrogen generation at the cathode for simultaneous production of high-valued chemicals and fuels.

Recently, several electrocatalysts including phosphides,[12] selenides,[8,13] hydroxides,[14-16] and metal–organic frameworks (MOFs),[17] containing transition-metal-active sites (like Ni, Fe, and Co), have been developed for the BA oxidation reaction. Illustratively, it is well known that the surface reconstruction phenomenon of these electrocatalysts during the reaction produces much more active sites for the catalytic reaction.[18-23] During the electrochemical oxidation of BA molecules, cations with a high valence state are generated, which activate the reactant and yield promising conversion efficiency toward the target product. For instance, Ni-based electrocatalysts are widely used due to the on-site generation of the Ni^{2+}/Ni^{3+} couple,[17] which can be regarded as a redox mediator to accelerate the BA oxidation

to BN. The Ni^{2+} can be easily oxidized to NiOOH as an active site for BA oxidation under alkaline aqueous conditions.[8,24] Therefore, a rational catalyst design strategy that includes a metal-active site with reversible redox property still deserves further investigation.

Over the past few decades, two-dimensional (2D) metal phosphorous trichalcogenides (MPX_3) have attracted tremendous research attention due to their van der Waals layered feature, high surface area, and atomic-level thickness.[25,26] Over the past few years, their applications in electrocatalytic processes such as hydrogen evolution reaction,[27,28] oxygen evolution reaction (OER),[29] and oxygen reduction reaction have been explored.[30] Apart from these reactions, our group has recently explored the co-production of H_2 and N-benzylidenebenzylamine on 2D layered $In_{4/3}P_2Se_6$ nanosheet surfaces utilizing photocatalytic routes,[31] which highlights the potential application of MPX_3 in organic synthesis. Meanwhile, design of MPX_3-based materials as a solid solution ($M_{(1-x)}N_xPX_3$, where M and N are metals) is still intriguing since the involvement of the second metal could regulate the conductivity and electronic structure of MPX_3 materials.[32] In particular, for Ni-based catalysts, Fe doping has demonstrated the ability to promote the formation of active NiOOH species and improve the catalytic activity.[33-36] Considering the aforementioned works as a foundation, we anticipate that bimetallic MPX_3 nanostructures that possess Ni and Fe could be utilized for BA oxidation to BN. We first utilize density functional theory (DFT) calculations to evaluate the possibility of realizing Fe-doped $NiPS_3$ from a theoretical perspective (Figure S1). The high spin density and charge density could indicate higher electrical conductivity (Figure S2), which could eventually be beneficial for electrocatalytic reactions. This is further confirmed by the partial density of state and total density of state calculations shown in Figure S3, where the presence of Fe increases the density

of state around the Fermi level, which facilitates easier electron transfer. Additionally, the presence of Fe in the $NiPS_3$ structure significantly reduces the Ni vacancy formation energy, highlighting the crucial role of Fe in leaching Ni atoms and potentially facilitating the formation of the NiOOH structure.

In this work, we show that the facile surface transformation of $Ni_{(1-x)}Fe_xPS_3$ $(0 \leq x \leq 1)$ nanosheet array into Ni-FeOOH species facilitates the oxidation of BA to BN. The surface of $Ni_{0.89}Fe_{0.11}PS_3$ is modified to produce the Ni-FeOOH/$Ni_{0.89}Fe_{0.11}PS_3$ heterointerface, which is facilitated by an electrochemical activation process under alkaline conditions (Figure 1A). The moderate Fe-doped $NiPS_3$ (namely, $Ni_{0.89}Fe_{0.11}PS_3$) achieves the highest BN yield and Faradaic efficiency (FE) of 10.2 mg/h and 48.88%, respectively. Post-reaction characterizations of $Ni_{0.89}Fe_{0.11}PS_3$ reveal that the electrocatalyst undergoes partial oxidation when the electrocatalytic BA oxidation is carried out at 1.45 V vs. reversible hydrogen electrode (RHE), and this is accompanied by the generation of NiFeOOH active species. Interestingly, the as-formed NiFeOOH/$Ni_{0.89}Fe_{0.11}PS_3$

heterostructure is favorable for the oxidation of BA to BN. DFT calculations reveal that the incorporation of Fe into $NiPS_3$ promotes the generation of the active species NiOOH and facilitates the formation of the metal oxyhydroxide/ metal phosphorus trichalcogenide interface for BA oxidation. Additionally, it has been found that the BA oxidation mechanism advances through the formation of C_6H_5–CH–NH* rather than the C_6H_5–CH$_2$–N* intermediate, with the formation of the C_6H_5–CH–N* intermediate being identified as the rate-determining step (RDS). This study underscores the significant role of Fe in the electrocatalytic oxidation of Ni-based catalysts, providing a new strategy for the rational design of catalysts in nitrile synthesis using MPX_3-based materials.

2 | RESULTS AND DISCUSSION

A series of $Ni_{(1-x)}Fe_xPS_3$ $(0 \leq x \leq 1)$ electrocatalysts with varying stoichiometric ratios were synthesized using a solvothermal, followed by the space-confined chemical
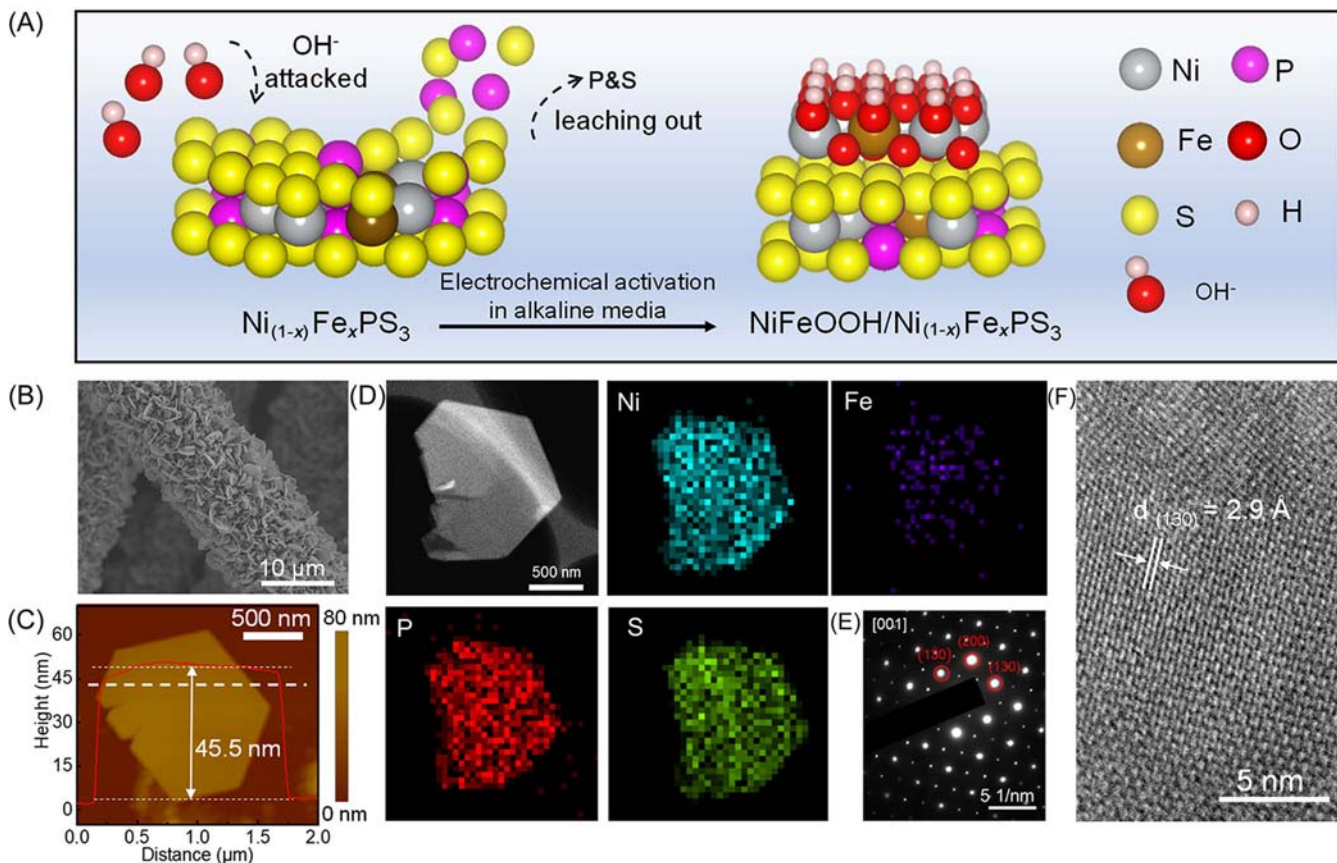

FIGURE 1 Structural and compositional characterizations of $Ni_{0.89}Fe_{0.11}PS_3$ nanosheets. (A) Schematic illustration of the formation of the NiFeOOH/$Ni_{(1-x)}Fe_xPS_3$ heterointerface on a $Ni_{(1-x)}Fe_xPS_3$ nanosheet during electrochemical activation in 1 M KOH. (B) SEM image of $Ni_{(1-x)}Fe_xPS_3$ nanosheet arrays on carbon cloth. (C) AFM image and the height profile collected from a single $Ni_{0.89}Fe_{0.11}PS_3$ nanosheet. (D) Corresponding elemental mapping images confirming a Ni, Fe, P, and S atomic ratio of 20.07:2.52:19.11:58.3. (E, F) SAED pattern and HR-TEM image of the as-synthesized $Ni_{0.89}Fe_{0.11}PS_3$ nanosheet.

vapor conversion method. Initially, the $Ni_{(1-x)}Fe_x(OH)_y$ ($0 \leq x < 1$) precursors were prepared on a carbon cloth substrate using a solvothermal process (Figures S4–S6). Subsequently, the as-prepared precursors were converted into $Ni_{(1-x)}Fe_xPS_3$ using a space-confined chemical vapor conversion method in a dual-temperature zone tube furnace (Figure S7). Note that the $FePS_3$ was synthesized as a control sample by utilizing an FeS_x precursor (Figure S6) instead of $Fe(OH)_y$ due to difficulty of achieving complete conversion of $Fe(OH)_y$ into $FePS_3$. As depicted in the scanning electron microscope (SEM) images (Figures 1B and S8–S10), the $Ni_{(1-x)}Fe_xPS_3$ hexagonal nanosheets are uniformly grown on the carbon cloth substrate. The corresponding energy-dispersive X-ray spectroscopy (EDX) analysis further reveals the atomic ratio of Ni, Fe, P, and S of the as-synthesized samples. The content of Ni and Fe was confirmed by EDX and an inductively coupled plasma-optical emission spectrometer (Tables S1 and S2). From the atomic force microscope (AFM) image in Figure 1C, it is clear that the representative $Ni_{0.89}Fe_{0.11}PS_3$ nanosheet has a thickness

of ~45.5 nm. The transmission electron microscopy (TEM) image and its corresponding elemental mapping (Figure 1D) demonstrate that Ni, Fe, P, and S with an atomic ratio of 20.07:2.52:19.11:58.3 are uniformly distributed throughout the entire $Ni_{0.89}Fe_{0.11}PS_3$ nanosheet. In addition, clear lattice fringes of $(1\bar{3}0)$, (200), and (130) are evidenced from the selected area electron diffraction (SAED) image of $Ni_{0.89}Fe_{0.11}PS_3$ nanosheets, indicating their good crystallinity. Further, the high-resolution transmission electron microscope (HR-TEM) image displays clear lattice fringes with a lattice spacing of 2.9 Å corresponding to (130) crystal planes, which is consistent with the SAED results (Figure 1E,F).

Figure 2A presents the X-ray diffraction (XRD) patterns of the as-synthesized $Ni_{(1-x)}Fe_xPS_3$ nanosheet samples. The diffraction patterns of $Ni_{(1-x)}Fe_xPS_3$ ($0 \leq x \leq 1$) samples indicate that the introduction of Fe into $NiPS_3$ does not change the crystal structure of $NiPS_3$ (PDF#33-0592). However, the relatively intense peak located at 13-15° corresponding to the (001) crystal plane reveal a gradual shift toward a lower position (2θ) with

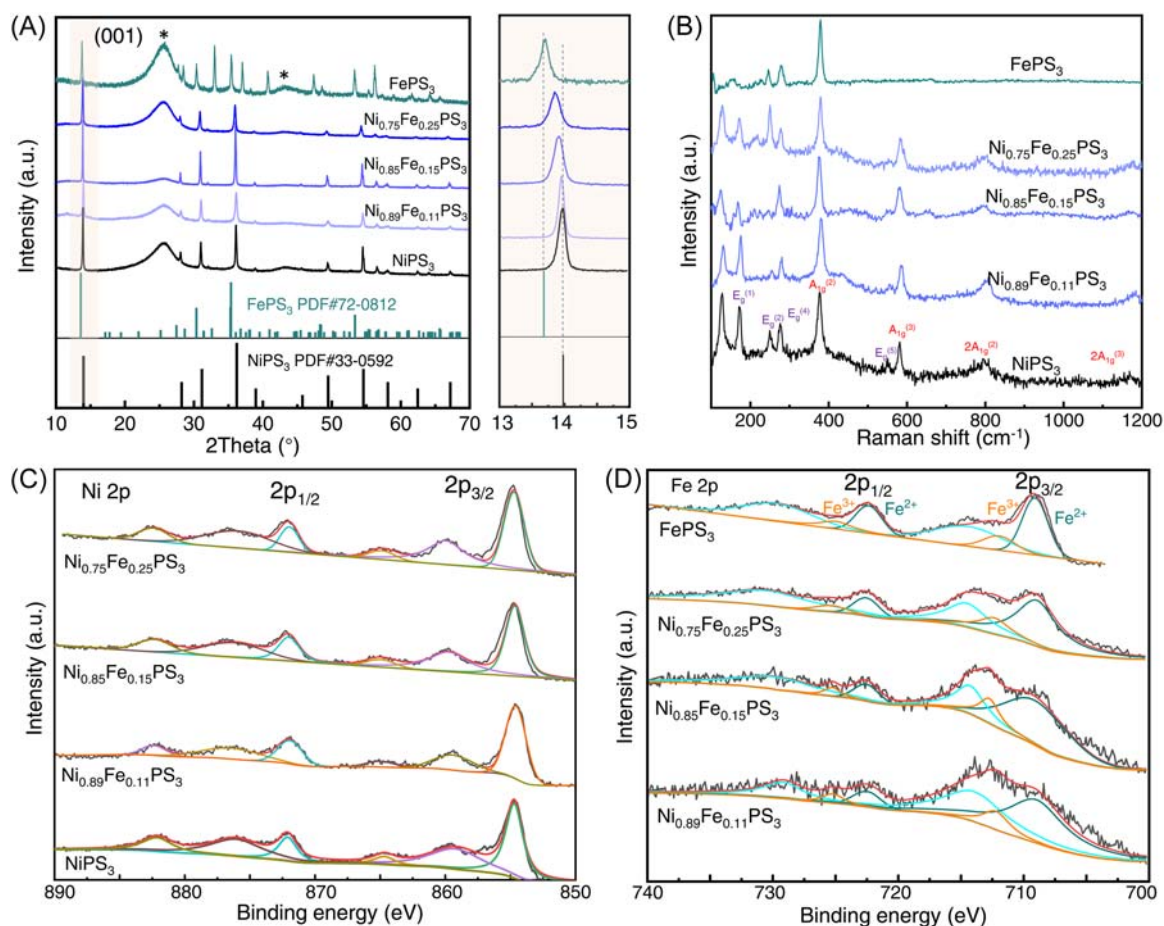

FIGURE 2 Structural and surface chemical characterizations of as-synthesized samples. (A) XRD patterns and (B) Raman spectra of the as-prepared $NiPS_3$, $FePS_3$, and $Ni_{(1-x)}Fe_xPS_3$ samples (the symbols * in (A) represent the XRD signals from the carbon cloth substrate). XPS spectra of (C) Ni 2p and (D) Fe 2p for the as-prepared $NiPS_3$, $FePS_3$, and $Ni_{(1-x)}Fe_xPS_3$ samples.

increasing Fe content. This shift can be attributed to the partial replacement of a smaller atomic radius Ni (0.69 Å for Ni^{2+}) by larger Fe (0.78 Å for Fe^{2+}). Note that the substitution of Ni by Fe also leads to a relatively larger lattice spacing (6.33 vs. 6.42 Å).[32] The Raman spectra of $Ni_{(1-x)}Fe_xPS_3$ ($0 \leq x \leq 1$) samples reveal the presence of four in-plane (E_g, 129.8, 174.1, 279.1, and 554.6 cm^{-1}) and four out-of-plane (A_{1g}, 378.8, 581.8, 805.2, and 1183.0 cm^{-1}) vibrations of $NiPS_3$, which corresponds to the P–S vibrations of the $[P_2S_6]^{4-}$ unit (Figure 2B).[32,37] It is noteworthy that all the $Ni_{(1-x)}Fe_xPS_3$ samples show Raman signals similar to those of $NiPS_3$, providing further evidence for the preserved crystal structure of $NiPS_3$ even after Fe incorporation. In contrast to the Raman signals of $NiPS_3$, the pristine $FePS_3$ displays three distinct peaks at 245, 277.4, and 377.8 cm^{-1}. These peaks are attributed to the vibration of P–P and P–S bonds within the $[P_2S_6]^{4-}$ unit.[28] X-ray photoelectron spectroscopy (XPS) was further utilized to determine the valence states of different metal ions in the as-synthesized $Ni_{(1-x)}Fe_xPS_3$ with varying Fe content. The XPS survey spectra offer clear evidence for the existence of Fe, Ni, P, and S elements in $Ni_{(1-x)}Fe_xPS_3$ ($0 \leq x \leq 1$), and the presence of P, S, and Ni or Fe, in the pristine $NiPS_3$ or $FePS_3$ samples (Figures S9 and S10). The Ni 2p XPS analysis (Figure 2C)

shows the peaks centered at 871.8 and 854.6 eV, which are assigned to $2p_{3/2}$ and $2p_{1/2}$ of Ni^{2+}, respectively. Additionally, two satellite peaks are evident at 859.4 and 864.7 eV. In the Fe 2p XPS spectra, the peaks centered at 708.7 and 722.8 eV are associated with $2p_{3/2}$ and $2p_{1/2}$ of Fe^{2+}, respectively. The two peaks at 712 and 725 eV are, respectively, ascribed to $2p_{3/2}$ and $2p_{1/2}$ of Fe^{3+}, which is due to the Fe^{2+} oxidized by air (Figure 2D).[38] Another signal at 713.3 eV corresponds to the satellite peak of Fe^{2+} $2p_{3/2}$.[39] The XPS spectra of P and S (both $2p_{1/2}$ and $2p_{3/2}$) in the $Ni_{(1-x)}Fe_xPS_3$ sample show a shift to a higher binding energy,[32] which may be due to the increased content of Fe^{2+} in $Ni_{(1-x)}Fe_xPS_3$ because of the different electronegativities of Fe^{2+} (1.292) and Ni^{2+} (1.367) (Figure S11).

Despite the growing interest in exploring the catalytic activity of novel MPX_3 for OER catalysis in alkaline media,[32,40,41] studies have shown that their potential application in organic chemical conversion is rare. In this work, BA electro-oxidation to BN is chosen as a model reaction to investigate the catalytic performance of $Ni_{(1-x)}Fe_xPS_3$ catalysts. Figure 3A presents the polarization curves collected from the $Ni_{(1-x)}Fe_xPS_3$ nanosheet electrode in a 1 M KOH electrolyte containing 20 mM BA. Compared with the other electrodes, including
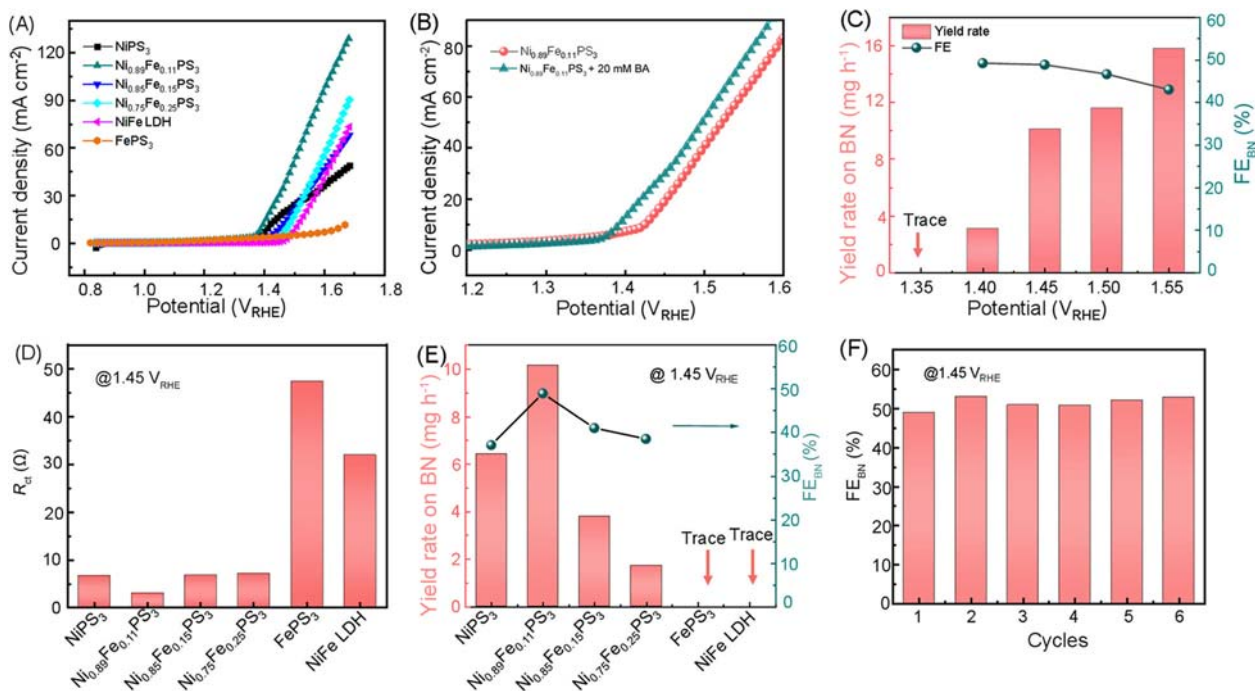

FIGURE 3 Electrocatalytic properties of BA oxidation to BN over $Ni_{(1-x)}Fe_xPS_3$ nanosheet electrodes. (A) LSV curves of the as-prepared $NiPS_3$, $FePS_3$, and $Ni_{(1-x)}Fe_xPS_3$ samples in 40 mL of 1 M KOH containing 20 mM BA. (B) Comparison of LSV curves of the $Ni_{0.89}Fe_{0.11}PS_3$ sample in 40 mL of 1 M KOH with (green) and without 20 mM BA (red). (C) FE values and yield rates for BN production through BA oxidation at different potentials. (D) Values of charge-transfer resistance determined from the EIS Nyquist plots of various $Ni_{(1-x)}Fe_xPS_3$, $FePS_3$, and $NiPS_3$ nanosheet electrodes. (E) Comparison of FE and yield rate of BN synthesis of the as-prepared $NiPS_3$, $FePS_3$, and $Ni_{(1-x)}Fe_xPS_3$ electrodes. (F) Cyclability of BN synthesis through BA oxidation over the $Ni_{0.89}Fe_{0.11}PS_3$ electrode under 1.45 V_{RHE}.

NiPS$_3$, NiFe layered double hydroxide (LDH), FePS$_3$ electrocatalysts, and so forth, the Ni$_{0.89}$Fe$_{0.11}$PS$_3$ nanosheet electrode shows the lowest onset potential of 1.39 V versus RHE (Figure 3B) and the smallest Tafel slope (59 mV dec^{-1}, Figure S12). Note that, in the absence of BA, the Ni$_{0.89}$Fe$_{0.11}$PS$_3$ electrocatalyst displays a relatively higher onset potential (1.43 V$_{RHE}$) and larger charge-transfer resistance (R_{ct}, 8.57 Ω) than that tested in the presence of BA (2.69 Ω) (Figure S13). Additionally, the operando electrochemical impedance spectroscopy (EIS) in Figure S14A,C shows that the R_{ct} decreased with increasing potentials both with and without BA, while the frequency with BA is significantly higher than that without BA, suggesting that BA oxidation with a higher reaction rate is preferred compared to the competing OER on the Ni$_{0.89}$Fe$_{0.11}$PS$_3$ electrocatalyst.[42] Linear scan voltammetry (LSV) tests are then conducted in 1 M KOH with different BA concentrations from 5 to 100 mM, and it can be seen that the current density increases as the BA concentration increases to 20 mM (Figure S15). However, a further increase in the BA concentration leads to a decrease in current density, which is possibly due to the decreased ion conductivity of the electrolyte and the limited product desorption. Next, the BA oxidation on the Ni$_{0.89}$Fe$_{0.11}$PS$_3$ electrode was evaluated by performing chronoamperometry measurements at constant potentials (1.35–1.55 V$_{RHE}$). A total charge of 77 C was allowed to pass through the anolyte of an H cell, which is separated from the catholyte with Nafion 117 as a membrane (Figure S16). The qualitative identification of BA oxidation products using the nuclear magnetic resonance (^{1}H NMR) technique shows that the signals of the target product BN are detected (Figure S17).[43] The yield of the BA oxidation product was quantified by gas chromatography (GC) tests using dodecane as an internal standard, and the corresponding FE values were determined (Figure S18). Figure 3C displays the potential-dependent yield rate and FE for BN production. When applying the potential from 1.35 to 1.55 V, the yield rate for BN synthesis increases accordingly. Also, the FE value reaches a higher value of 48.88% at a potential of 1.45 V$_{RHE}$ with a yield rate of 10.15 mg/h, while the FE value gradually decreases on further increasing the potential from 1.45 to 1.55 V$_{RHE}$. However, the yield rate of BN increased with increasing potential as the current density increased (Figure S19). The decrease in FE at a potential above 1.45 V could be due to the competing OER, which became the prominent reaction, and the poor desorption of the oxidation products on the surface of the catalysts, as the frequency peak decreased with increasing potentials in the operando EIS (Figure S14B,D).[13,44]

To further explore the catalytic activity of the as-prepared Ni$_{(1-x)}$Fe$_x$PS$_3$ electrocatalysts, EIS measurements

at 1.45 V$_{RHE}$ were performed (Figure 3D). It is observed that Ni$_{0.89}$Fe$_{0.11}$PS$_3$ shows the smallest charge-transfer resistance of 2.69 Ω for BA oxidation compared with all other variants (Figures 3D and S20). The highest BN yield rate and FE value through BA oxidation are obtained on the Ni$_{0.89}$Fe$_{0.11}$PS$_3$ nanosheet electrode (Figure 3E). It is noteworthy that, compared with the pure NiPS$_3$ and FePS$_3$ electrocatalysts, the Ni$_{0.89}$Fe$_{0.11}$PS$_3$ electrode demonstrates superior performance. This suggests that the moderate doping of Fe into NiPS$_3$ has a beneficial effect on enhancing its electrocatalytic activity. Besides, it is well-documented that phosphide- and sulfide-based materials undergo surface oxidation during OER catalysis, which gives rise to the formation of oxide or oxyhydroxide species on their surface. Thus, we also evaluate the intrinsic electrocatalytic activity of NiFe LDH as a control sample for BA oxidation, which shows inferior catalytic activity toward BA oxidation. To further understand the crucial role of P and S, the electrochemical performance of the NiFe LDH control was examined in a 1 M KOH electrolyte containing 0.1 M K$_2$SO$_4$ and 0.1 M K$_3$PO$_4$ at a potential of 1.45 V$_{RHE}$. Notably, similar to the previous test in the absence of 0.1 M K$_2$SO$_4$ and 0.1 M K$_3$PO$_4$ additives (Figure 3E), only a trace amount of BN was detected when the NiFe LDH electrode was examined in the electrolyte containing 0.1 M K$_2$SO$_4$ and 0.1 M K$_3$PO$_4$. This result suggests that the performance of NiFe LDH remains unchanged in solutions containing phosphates and sulfates, which substantiates our claim that the heterointerface has contributed to the observed performance. Additionally, to further illustrate the role of P and S in Ni$_{0.89}$Fe$_{0.11}$PS$_3$, the BA oxidation performance of NiFeS and NiFeP was also determined as control samples. As shown in Figure S21, both NiFeP and NiFeS showed lower current densities compared to Ni$_{0.89}$Fe$_{0.11}$PS$_3$, indicating the low electrocatalytic BA oxidation activity of NiFeS and NiFeP. Accordingly, the FE values for BN synthesis through BA oxidation over NiFeS and NiFeP are lower than that in Ni$_{0.89}$Fe$_{0.11}$PS$_3$, indicating that both P and S in Ni$_{0.89}$Fe$_{0.11}$PS$_3$ play important roles in the electrocatalytic oxidation of BA to BN, which also demonstrates the unique and superior properties of this material. Finally, the stability of the Ni$_{0.89}$Fe$_{0.11}$PS$_3$ electrocatalyst was evaluated by applying the same potential of 1.45 V$_{RHE}$ for 6 consecutive cycles (each cycle with 77 C charge). The continuous electrolysis of BA over Ni$_{0.89}$Fe$_{0.11}$PS$_3$ within ~7 h shows that the FE for BN synthesis could be maintained at 52.8%, demonstrating its good stability.

To unravel the mechanism of BA oxidation over Ni$_{(1-x)}$Fe$_x$PS$_3$ electrodes, post-reaction characterizations were conducted. The XPS analysis of Ni$_{0.89}$Fe$_{0.11}$PS$_3$ after

BA oxidation reveals a shift toward higher binding energy for Ni^{2+} compared with the fresh sample. The peaks at 857.3 and 874.7 eV in Ni 2p XPS of this sample respectively originate from $2p_{3/2}$ and $2p_{1/2}$ of Ni^{3+}, while the peaks located at 712.5 and 725.5 eV in Fe 2p XPS spectrum originate from Fe^{3+} 2p (Figure 4A,B). Notably, only Ni^{2+} was present in the fresh $Ni_{0.89}Fe_{0.11}PS_3$, 28% of Ni^{3+} was generated, and Ni^{2+} decreased from 100% to 72%. For the Fe 2p, Fe^{2+} was decreased from 85% to 75%, while Fe^{3+} increased from 15% to 25%, indicating the partial oxidation of the $Ni_{0.89}Fe_{0.11}PS_3$ surface during the BA oxidation reaction. The O 1s spectrum of $Ni_{0.89}Fe_{0.11}PS_3$ after the reaction (Figure S22) clearly shows the presence of Ni(Fe)–O, OH, and S–O bonds, suggesting the formation of high-valent NiFeOOH on the surface of $Ni_{(1-x)}Fe_xPS_3$[45–47] after BA oxidation catalysis. To further examine the changes in electronic properties, the valence band maximum (VBM) of $Ni_{0.89}Fe_{0.11}PS_3$ before and after BA oxidation was examined using XPS valence band spectra tests. As shown in Figure 4C, the VBM of $Ni_{0.89}Fe_{0.11}PS_3$ decreased from 2.42 eV (fresh sample) to 1.32 eV (after reaction), indicating an improvement in

the electronic conductivity of $Ni_{0.89}Fe_{0.11}PS_3$,[15,48] which would be more beneficial during the electrocatalytic BA oxidation. Further, the TEM images collected from the $Ni_{0.89}Fe_{0.11}PS_3$ nanosheet after BA oxidation show that the nanosheet morphology is not altered after the reaction. However, a clear polycrystalline diffraction ring corresponding to (112) and (200) facets of the Ni(Fe)OOH crystal is seen in the SEAD image, suggesting the possible formation of oxyhydroxide on the parent $Ni_{0.89}Fe_{0.11}PS_3$. Complementary to this, the HR-TEM image in Figure 4D reveals the co-existence of the (200) and (001) facets of Ni(Fe)OOH and the (130) facet of $Ni_{0.89}Fe_{0.11}PS_3$, confirming the generation of the $NiFeOOH/Ni_{0.89}Fe_{0.11}PS_3$ heterointerface during BA oxidation. This suggests the surface transformation of the $Ni_{0.89}Fe_{0.11}PS_3$ precatalyst into a catalytically active $NiFeOOH/Ni_{0.89}Fe_{0.11}PS_3$ heterostructure, which accounts for the improved activity in terms of BN synthesis. Additionally, the SEM images (Figure S23) and the TEM-EDX elemental mapping (Figure 4E) show the presence and uniform distribution of Ni, Fe, P, S, and O throughout the nanosheet. Note that the surface of $Ni_{0.89}Fe_{0.11}PS_3$ becomes rough after BA
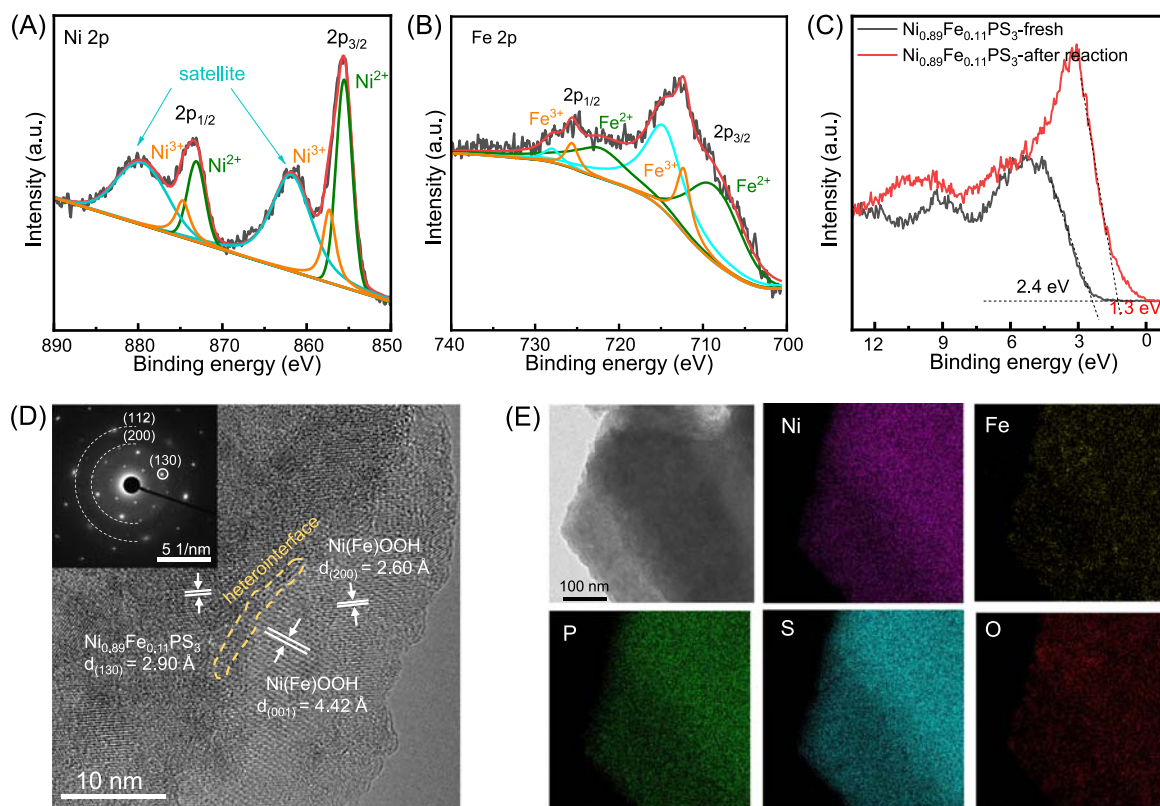

FIGURE 4 Morphological and structural characterizations of $Ni_{0.89}Fe_{0.11}PS_3$ after the BA oxidation reaction for 1 h at 1.45 V_{RHE}. XPS spectra of (A) Ni 2p and (B) Fe 2p of $Ni_{0.89}Fe_{0.11}PS_3$ after 1 h of BA oxidation catalysis. The 1 M KOH was used as an electrolyte and 20 mM BA was utilized as the initial reactant concentration. (C) Comparison of the XPS valence band spectra of $Ni_{0.89}Fe_{0.11}PS_3$ before (black) and after (red) BA oxidation. (D) HR-TEM image of $Ni_{0.89}Fe_{0.11}PS_3$ after 1 h of BA oxidation catalysis. The inset shows the corresponding SAED image. (E) TEM elemental mapping images of $Ni_{0.89}Fe_{0.11}PS_3$ after BA oxidation at 1.45 V_{RHE} for 1 h.

oxidation catalysis, while no appreciable change is observed in its morphology. A distinct peak at ~467 cm^{-1} that accounts for the formation of NiFeOOH is observed in the Raman spectra of $Ni_{0.89}Fe_{0.11}PS_3$ after BA oxidation at 1.4 V_{RHE}, indicating catalyst surface transformation into NiFeOOH on the $Ni_{0.89}Fe_{0.11}PS_3$ nanosheet. The collected XRD patterns on the $Ni_{0.89}Fe_{0.11}PS_3$ sample after the reaction at 1.45 V_{RHE} show only decreased peak intensity, but the $Ni_{0.89}Fe_{0.11}PS_3$ structure is still retained, which could be due to the poor crystallinity of the as-formed NiFeOOH species on the catalyst surface (Figure S24A). Further, potential-dependent XRD and Raman characterizations (ex situ) were conducted at applied potentials from 1.4 V to 1.55 V_{RHE} (Figure S24). It is demonstrated that the diffraction peaks of $Ni_{0.89}Fe_{0.11}PS_3$ almost disappeared at the potential of 1.55 V_{RHE} after a 0.56 h reaction. Ex situ Raman characterizations demonstrate two additional new peaks at ~476 and ~556 cm^{-1}, originating from Ni–OOH, and new peaks at ~670 and ~696 cm^{-1} originating from S–O and FeOOH.[49,50] This result suggests that the $Ni_{0.89}Fe_{0.11}PS_3$ nanosheet is completely transformed into NiFeOOH at 1.55 V_{RHE}, while the potential ~1.45 V_{RHE} causes only partial transformation of the initial catalyst. Combining the aforementioned results, it can be concluded that the surface of $Ni_{0.89}Fe_{0.11}PS_3$ is partially oxidized during the electrocatalytic oxidation of BA, leading to surface reconstruction to form a NiFeOOH/$Ni_{0.89}Fe_{0.11}PS_3$ heterostructure. When the applied potential is 1.4 V_{RHE}, the primarily oxidized $Ni_{0.89}Fe_{0.11}PS_3$ surface serves as an active site to oxidize BA to BN.[51] As the potential increases to 1.45 V_{RHE}, the BA oxidation reaction becomes predominant and the generated NiFeOOH/$Ni_{0.89}Fe_{0.11}PS_3$ heterostructure accounts for the higher conversion efficiency of BA. However, with a further increase in potential, the OER reaction becomes dominant and complete transformation of $Ni_{0.89}Fe_{0.11}PS_3$ into NiFeOOH is observed. The corresponding decline in the FE of BN is mainly due to the competing OER. This evidences the crucial role of the as-formed NiFeOOH/$Ni_{0.89}Fe_{0.11}PS_3$ heterostructure for the conversion of BA into BN.

To further investigate the surface reconstruction of $Ni_{0.89}Fe_{0.11}PS_3$ during electrocatalytic BA oxidation, chronoamperometry tests were conducted in 1 M KOH containing different concentrations of BA. A total charge of 77 C was passed through the electrolyte during the experiment. Figure S25 shows the FE and yield rate of BN for the conversion of 5 mM and 20 mM BA as initial concentrations. It is interesting to note that at a low BA concentration (5 mM), the catalyst surface is primarily enriched with OH, and the OER dominates, leading to the complete conversion of $Ni_{0.89}Fe_{0.11}PS_3$ into NiFeOOH (SEM and EDX in Figure S26, and XRD and Raman spectra in Figure S27). Consequently, the FE for BN production is lower (30.86%). On the contrary, when the reactant concentration is 20 mM, the BA molecules are adsorbed on the electrode surface, and BA oxidation becomes dominant over the competing OER. In this case, the FE for BN synthesis is higher and the catalyst surface is less exposed to OH environment which protects it from being completely oxidized.

To elucidate the formation of the heterointerface described above, post-reaction catalyst characterizations were also performed on the $Ni_{0.89}Fe_{0.11}PS_3$ electrocatalyst after six consecutive cycles. As shown in Figure S28, the morphology of the catalyst remained unchanged, whereas the XRD patterns and Raman spectra (Figure S29) showed a decrease in intensity with increasing number of cycles. In the Raman spectra of this sample after three cycles, new Raman peaks corresponding to NiOOH and FeOOH began to appear. Additionally, the XPS analysis reveals a gradual shift of the Ni 2p and Fe 2p peaks toward higher binding energy with increasing cycles, whereas the P 2p and S 2p peaks shift toward lower binding energy with a significant decrease in the intensity. This suggests that $Ni_{0.89}Fe_{0.11}PS_3$ is oxidized to form NiFeOOH at the surface. Notably, the presence of P and S is further confirmed from XPS spectra and the TEM elemental mapping in Figures S30 and S31 after six cycles of operation. The additional peak at 135.0 eV in Figure S30C and 168.3 eV in Figure S30D can be ascribed to PO_4^{3-} and SO_4^{2-}, respectively,[52] indicating that some of the P and S in $Ni_{0.89}Fe_{0.11}PS_3$ were leached out and transferred to PO_4^{3-} and SO_4^{2-} and were absorbed on the surface of the material. In addition, the XRD pattern in Figure S29A indicates the retention of the $Ni_{0.89}Fe_{0.11}PS_3$ structure, providing additional evidence for the formation of the NiFeOOH/$Ni_{0.89}Fe_{0.11}PS_3$ heterostructure.[41] The above-detailed post-characterization results indicate the formation of NiFeOOH/$Ni_{0.89}Fe_{0.11}PS_3$, which accounts for the enhanced electrocatalytic activity for the synthesis of BN from BA.

To uncover the reaction mechanism of BA oxidation over $Ni_{0.89}Fe_{0.11}PS_3$ and the correlation between the structure and catalytic activity of the catalyst, DFT calculations were used. The reactivity of Fe-doped $NiPS_3$ toward the hydroxyl group (OH*), and the impacts of Fe on the surface reconstruction of $NiPS_3$ to NiOOH were first examined (Figure 5A,B). The adsorption energies of the OH* on $NiPS_3$, $Fe_{0.250}Ni_{0.750}PS_3$, and $Fe_{0.125}Ni_{0.875}PS_3$ models are presented in Figure 5B. It can be seen that the incorporation of Fe into $NiPS_3$ enhances the adsorption energy of OH and hence promotes the formation of NiOOH. Next, the adsorption energies of the reactant
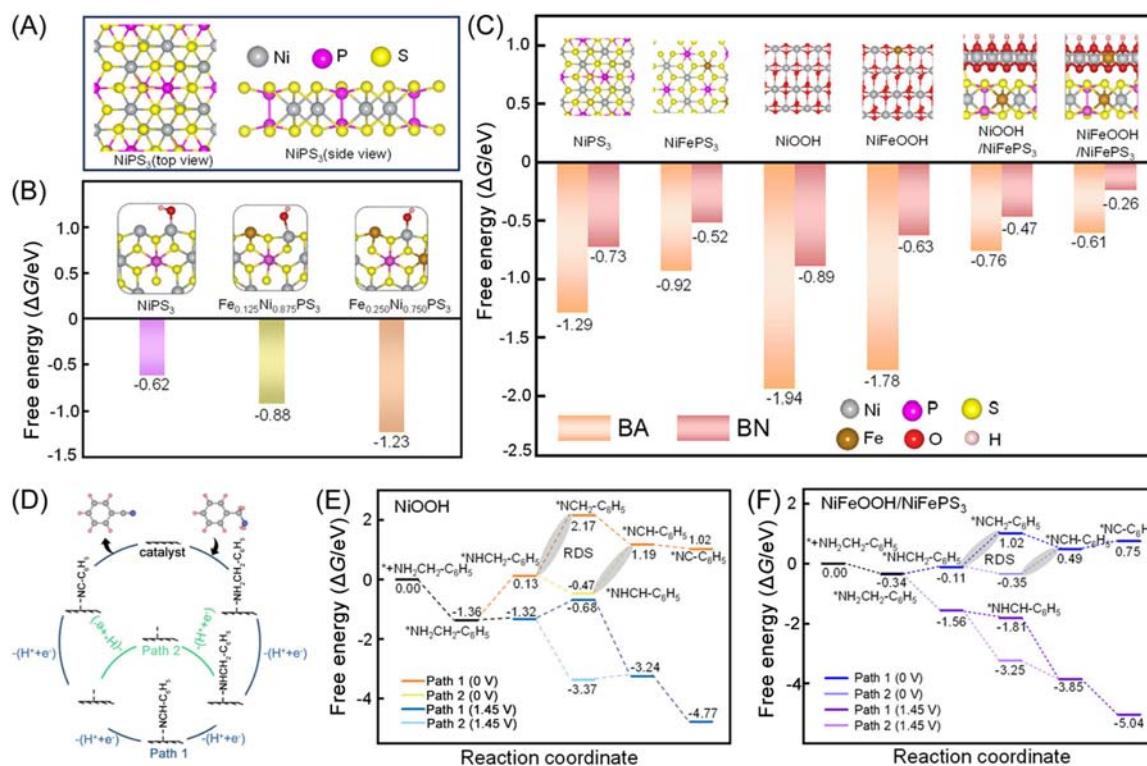
FIGURE 5 Theoretical investigation of the BA oxidation reaction mechanism on various electrocatalysts. (A) Optimized $NiPS_3$ model. (B) Adsorption energy of OH on $NiPS_3$, $Fe_{0.125}Ni_{0.875}PS_3$, and $Fe_{0.250}Ni_{0.750}PS_3$ models. (C) Adsorption energy of BA and BN on $NiPS_3$, $NiFePS_3$, $NiOOH$, $NiFeOOH$, $NiOOH/NiFePS_3$, and $NiFeOOH/NiFePS_3$ models. (D) Plausible reaction pathways for BA oxidation to BN. (E, F) Free energies during the BA oxidation reaction on (E) $NiOOH$ and (F) $NiFeOOH/NiFePS_3$ at a pH of 13.5.

(BA) and the product (BN) molecules on various models were calculated (Figure 5C). The calculated BA adsorption energies on $NiOOH$, $NiPS_3$, $NiFePS_3$, $NiFeOOH$, $NiOOH/FeNiPS_3$, and $FeNiOOH/FeNiPS_3$ are −1.94, −1.29, −0.92, −1.78, −0.76, and −0.61 eV, respectively, indicating that the BA molecular is adsorbed on these catalyst surfaces easily, especially on $NiOOH$. However, the adsorption of product BN on the pristine $NiOOH$ surface is also very strong, with a high adsorption energy of −0.89 eV, suggesting potential surface poisoning that could impede electro-oxidation of BA on $NiOOH$ due to the poor desorption of BN. In contrast, the hetero-interfaces of $FeNiOOH/FeNiPS_3$ yield optimum energy for BA adsorption (−0.61 eV) and BN desorption (−0.26 eV), which serves to fine-tune the activity of the catalyst to achieve the highest possible level of activity.

Based on the aforementioned results, the BA oxidation reaction pathways are examined using different models ($NiOOH$, $NiOOH/NiFePS_3$, and $NiFeOOH/NiFePS_3$ heterostructure). Initially, the most stable surface structure is determined under real working conditions for each model, and subsequently, a surface free-energy diagram is constructed with different monolayer (ML) coverages of H_2O, OH, and O as a function of the applied potential.

Specifically, the simulation was carried out by considering our experimental electrochemical operating conditions (pH = 13.5 and $U = 1.45\ V_{RHE}$). The result suggests that the $NiOOH$ surface could be covered with 1/3 ML H_2O and 2/3 ML OH, representing the most stable equilibrium surface (Figure S32), whereas the surfaces of $NiOOH/FeNiPS_3$ and $NiFeOOH/FeNiPS_3$ could be covered with 1 ML OH (Figure S33), and 2/3 ML OH and 1 ML O (Figure S34), respectively. Next, the reaction pathways for the dehydrogenation of BA were evaluated under the aforementioned optimized conditions (Figure 5D). Following the adsorption of the BA molecule, the initial dehydrogenation occurs to form the intermediate $C_6H_5-CH_2-NH^*$. Subsequently, two potential types of dehydrogenation processes take place: dehydrogenation of the N–H bond resulting in the formation of the $C_6H_5-CH_2-N^*$ intermediate (path 1) or breakage of the first C–H bond resulting in the formation of the $C_6H_5-CH-NH^*$ intermediate (path 2). These intermediates can then be converted into the $C_6H_5-CH-N^*$ intermediate, and the next dehydrogenation step occurs, which yields the product BN (C_6H_5-CN). To understand the reaction mechanism on the reconstructed surface, the free energies of each step in the oxidation of BA to BN on $NiOOH$, $NiFeOOH/NiFePS_3$, and $NiOOH/NiFePS_3$ models

are calculated (Figures 5E,F and S35). At a potential of $0 V_{RHE}$, the formation of both the C_6H_5–CH_2–N* intermediate (in path 1) and C_6H_5–CH–NH* (in path 2) occurs through exergonic processes for all three models. This implies that the two steps are the RDS of BA oxidation under the potential of $0 V_{RHE}$. The lowest energy barrier corresponding to C_6H_5–CH_2–N* and C_6H_5–CH–NH* suggests that NiFeOOH/NiFePS$_3$ has more favorable reaction kinetics than other surfaces, which indicates its better catalytic activity for BA oxidation. The reaction pathways were also evaluated considering the experimental potential of $1.45 V_{RHE}$. The NiFeOOH/NiFePS$_3$ heterostructure shows downhill energy barriers for each step compared with NiOOH and NiOOH/NiFePS$_3$, which further validates the experimental observation that the formation of the NiFeOOH/FeNiPS$_3$ heterostructure is essential to promoting the electro-oxidation of BA at pH = 13.5 and electrode potential of $1.45 V_{RHE}$.

The non-active-site P and S usually do not directly affect the catalytic activity, but they can influence the electronic structure of the catalyst. It is reported that a wide range of materials containing P and S would undergo surface reconstruction during the oxidation reaction, where P and S will be transformed into water-soluble (oxy)anions and adsorb on the surface of the catalyst, affecting the formation of intermediates in the OER reaction.[23,53–55] As shown in the XPS spectra of Ni$_{0.89}$Fe$_{0.11}$PS$_3$ after the reaction (Figure S30), some P and S in Ni$_{0.89}$Fe$_{0.11}$PS$_3$ leached out and transformed into PO_4^{3-} and SO_4^{2-}, which then adsorbed onto the catalyst surface. In order to investigate the effect of the reabsorption of PO_4^{3-} and SO_4^{2-} on BA oxidation, a control experiment and DFT calculations were conducted. The NiFe LDH without P and S was selected as the electrocatalyst for the control experiment; however, only trace amounts of BN were detected after BA oxidation as shown in 1 M KOH; it still showed inferior BA oxidation performance. Additionally, we conducted related theoretical calculations to further verify the influence of reabsorption of PO_4^{3-} and SO_4^{2-}. Figure S36 shows that despite variations in the charge density of Ni active sites of NiFeOOH/NiFePS$_3$ before and after adoption of SO_4^{2-} and PO_4^{3-} on the surface, it is evident that these ions do not significantly alter the electrochemical behavior of the Ni site, as there are no observable changes in charge density depletion or acquisition in the presence of these ions. Also, there were no significant changes in the BA adsorption and BN desorption energy in the presence of SO_4^{2-} or PO_4^{3-} ions (Figure S37). Finally, we examined the reaction mechanism to determine if the presence of SO_4^{2-} or PO_4^{3-} ions could impact the energy barrier of the BA oxidation reaction mechanism. As depicted in Figure S38, the oxidation of BA to BN proceeded via path 2 rather than path 1, similar to the original NiFeOOH/Ni$_{0.89}$Fe$_{0.11}$PS$_3$. The RDS still involved the transformation of NH-CH-C_6H_5 into N-CH-C_6H_5, and the energy required to obtain N–CH–C_6H_5 after adsorbing phosphate or sulfate ions did not change significantly.

3 | CONCLUSION

In summary, we have introduced a controllable design method to synthesize Ni$_{(1-x)}$Fe$_x$PS$_3$ electrocatalysts with different Fe dopants for electro-oxidation of aromatic amine. The intrinsic electrocatalytic activity of these catalysts and the catalytic mechanism are studied in depth by combining experimental and theoretical studies. During BA oxidation, the Ni$_{0.89}$Fe$_{0.11}$PS$_3$ electrocatalyst readily undergoes surface transformation to form an active and stable NiFeOOH/Ni$_{0.89}$Fe$_{0.11}$PS$_3$ heterostructure, which plays a key role in enhancing activity during BA oxidation to produce BN. Theoretical and experimental results suggest that the presence of Fe contributes to the surface transformation of Ni$_{0.89}$Fe$_{0.11}$PS$_3$ into NiFeOOH/Ni$_{0.89}$Fe$_{0.11}$PS$_3$. Interestingly, the complete conversion of Ni$_{0.89}$Fe$_{0.11}$PS$_3$ into NiFeOOH is mainly dependent on the type of reaction (OER or BA oxidation) that takes place on the catalyst surface. Furthermore, the BA oxidation reaction mechanism was investigated by the calculations, which identified the formation of the C_6H_5–CH–N* intermediate as the RDS. The as-formed NiFeOOH/Ni$_{0.89}$Fe$_{0.11}$PS$_3$ heterostructure shows more favorable reaction kinetics during the oxidation of BA to BN. Our study provides a new avenue for rational electrode design guided by an understanding of surface reconstruction, which could broaden the scope of various kinds of organic chemical synthesis.

4 | EXPERIMENTAL SECTION

4.1 | Synthesis of Ni$_{(1-x)}$Fe$_x$(OH)$_y$ nanosheets

Ni$_{(1-x)}$Fe$_x$(OH)$_y$ nanosheets were synthesized using a hydrothermal method.[56] Typically, 3 mmol of Ni(NO$_3$)$_2$·6H$_2$O and Fe(NO$_3$)$_3$·9H$_2$O in different molar ratios, 6 mmol of NH$_4$F, and 15 mmol of CO(NH$_2$)$_2$ were dissolved in 35 mL of ultrapure water. The mixture was then stirred for 15 min to form a homogeneous solution. The molar ratio of Ni(NO$_3$)$_2$·6H$_2$O to Fe(NO$_3$)$_3$·9H$_2$O was varied for the preparation of Ni$_{(1-x)}$Fe$_x$(OH)$_y$ nanosheets with different Ni/Fe ratios. Then, the uniform solution was transferred to a 50 mL Teflon reactor. Subsequently,

a cleaned carbon cloth $2 \times 4\,cm^2$ in size was immersed in the solution. Finally, an autoclave was heated at 120°C for 6 h. After the reaction was complete, the obtained $Ni_{(1-x)}Fe_x(OH)_y$ nanosheets loaded on carbon cloth were washed with absolute ethanol three times and with ultrapure water three times and then dried overnight at 60°C in a hot-air oven.

4.2 | Synthesis of FeS_x precursor

First, 2 mmol of $FeCl_3 \cdot 6H_2O$ and 2.4 mmol of CH_2NSCH_3 were dissolved in a mixture of 20 mL of absolute ethanol and 10 mL of water. Then, the solution was sonicated for 20 min to ensure the total dissolution of $FeCl_3 \cdot 6H_2O$. Subsequently, the resulting solution was transferred to a 50 mL Teflon autoclave, where a cleaned carbon cloth was immersed in the solution, followed by a solvothermal reaction at 150°C for 2 h. After the reaction was completed, the reactor was allowed to cool naturally. Finally, the as-grown FeS_x was washed multiple times with ethanol and water and then dried overnight at 60°C in a vacuum oven.[57]

4.3 | Synthesis of $Ni_{(1-x)}Fe_xPS_3$ nanosheets

$Ni_{(1-x)}Fe_xPS_3$ nanosheets on carbon cloth with different molar ratios were synthesized by a space-confined chemical vapor conversion process using the synthesized $Ni_{(1-x)}Fe_x(OH)_y$ nanosheets as a precursor in a tube furnace with two zones (Figure S7). Typically, a stoichiometric mixture of P and S powders (0.5 g in total and a P:S ratio of 1:3) was placed at Zone I of the tube furnace, while a carbon cloth loaded with the $Ni_{(1-x)}Fe_xPS_3$ precursor (or FeS_x) was placed at Zone II; the distance between the two zones was about 20 cm. Before the reaction, the tube system was purged by argon gas at a flow rate of 100 sccm and vacuumed to create an air-free atmosphere. Then, the two zones were simultaneously heated to 280°C and 500°C, respectively, within 30 min. Zone I was heated to 300°C within 90 min, while Zone II was maintained at 500°C, and the flow rate of argon gas was maintained at 20 sccm during the reaction. Finally, the furnace was naturally cooled to room temperature, and the carbon cloth with $Ni_{(1-x)}Fe_xPS_3$ nanosheets was taken out for further measurement.

4.4 | Material characterizations

The thickness and morphology of $Ni_{(1-x)}Fe_xPS_3$ nanosheets were characterized by AFM (Bruker-M8) and field emission SEM (Hitachi SU8220), respectively. HRTEM (JEM-2100F) equipped with an energy-dispersive X-ray diffractometer (EDX) was also used. The metal content in the sample was quantitatively determined using inductively coupled plasma mass spectrometry (Agilent 5100 ICP-OES). The crystal structure was investigated by XRD (TZY-XRD (D/MAX-TTRIII (COB))) using Cu-Kα radiation. Raman spectra were collected on a Raman microscope (Renishaw, In Via) with a 532 nm excitation laser. XPS was performed on an X-ray photoelectron spectrometer (ESCALab 250Xi) with an X-ray source (Mg Kα) to determine the elemental composition and valence states of the samples, as well as the VBM of $Ni_{0.89}Fe_{0.11}PS_3$ before and after the reaction. All the binding energies were referenced to the C 1s peak at 284.8 eV. In particular, the $Ni_{0.89}Fe_{0.11}PS_3$ on carbon cloth was directly used as an electrode for the electrochemical tests; then, the electrode was cleaned and dried for the XPS VBM spectrum test. The exact values of the VBM of $Ni_{0.89}Fe_{0.11}PS_3$ before and after the reaction were calculated using the following equation[58]:

$$E_{VB,NHE} = \varphi + E_{VB} - 4.44, \tag{1}$$

where $E_{VB,NHE}$ is the VBM of the $Ni_{(1-x)}Fe_xPS_3$, φ is the electron work function of the spectrometer (4.46 eV), and E_{VB-XPS} can be obtained from the VB-XPS spectrum.

4.5 | Electrochemical measurements

The electrochemical performance of a series of $Ni_{(1-x)}Fe_xPS_3$ samples was evaluated on an electrochemical workstation (Applied Research Potentiostat, Versa-STAT3) using a three-electrode system in an H-type cell. The Nafion 117 membrane was used as a separator. The Nafion 117 membrane was pretreated through a series of steps before use. First, the membrane was treated at 80°C in a 5 wt% H_2O_2 solution for 1 h to remove organic impurities. Next, it was thoroughly rinsed with deionized water and then immersed in deionized water at 80°C, where it was boiled for 1 h to ensure complete removal of the residual H_2O_2. Finally, the membrane was soaked in 1 M H_2SO_4 at 80°C for 1 h, followed by rinsing with deionized water to remove the remaining H_2SO_4. A Hg/HgO electrode, a Pt foil, and the $Ni_{(1-x)}Fe_xPS_3$ nanosheets grown on carbon cloth $1 \times 1\,cm^2$ in size were used as a reference, counter, and working electrodes, respectively. LSV and chronoamperometry tests were performed in a 1 M KOH (pH = 13.5) solution, where the scan rate was set as $5\,mV\,s^{-1}$. The activity of $Ni_{(1-x)}Fe_xPS_3$ catalysts in the electrocatalytic oxidation of

benzylamine was evaluated using chronoamperometry at different potentials (1.35–1.55 V_{RHE}). Before the LSV and chronoamperometry measurements, all samples were activated by 20 cyclic voltammetry (CV) cycles in the potential range of 0.8–1.6 V_{RHE}, for which the scan rate was 100 mV s^{-1}. All the potentials were calibrated to a RHE using the following equation: $E_{RHE} = E_{Hg/HgO} + 0.098 + 0.059 \times pH$, with 100% iR correction. EIS tests were performed at the potential of 1.45 V_{RHE} in the frequency range from 100 KHz to 0.01 Hz. The BA oxidation measurements were carried out over a series of $Ni_{(1-x)}Fe_xPS_3$ samples and NiFe LDH as a control. Unless specifically mentioned, the electrolysis was conducted in 40 mL of KOH with 20 mM BA as a reactant.

4.6 | Product analysis

First, a qualitative analysis of the BA electrocatalytic oxidation product was carried out by nuclear magnetic resonance (^{1}H NMR, Bruker Avance III 400 HD) using D_2O with dimethyl sulfoxide (DMSO) as the internal standard. To determine the corresponding yield rate and FEs of BN, 40 mL of electrolyte solution was extracted with ethyl acetate after chronoamperometry testing with a total passing charge of ~77 C. The extracted oxidation products were confirmed by GC measurements using dodecane as an internal standard. The temperature of the column was initially set at 70°C for 1 min and increased to 150°C at a rate of 10°C/min.[14] Then, the temperature was increased to 220°C at a rate of 25°C/min and maintained for 3 min. The yield and FE of BN were calculated using the following equations:

$$\text{Yield rate (mg h}^{-1}) = \frac{\text{m of formed benzonitrile}}{t}, \quad (2)$$

$$\text{FE (\%)} = \frac{\text{mol of benzonitrile}}{\text{total passed charge}/(4 \times F)} \times 100\%, \quad (3)$$

where m is the mass of the formed BN (mg); t is the reaction time of chronoamperometric tests; and F is the Faraday constant, 96,485 C mol^{-1}. The theoretical charge required for the complete conversion of 0.2 mmol BA to BN is ~77 C.

4.7 | Theoretical calculations

Spin-polarized DFT calculations with the Perdew–Burke–Ernzerhof (PBE) exchange–correlation functional[59] were performed using the Vienna ab initio simulation package (VASP).[60] The projector-augmented wave method (PAW)[61,62] with a plane-wave kinetic energy cutoff of 500 eV was used, with a Gaussian smearing of 0.05 eV.[63] The Brillouin zone was sampled by a $3 \times 3 \times 1$ K-point for geometry optimization and a $6 \times 6 \times 1$ K-point to calculate the spin density and charge density differences. Based on the experimental results, we used an eight-layer slab containing 8 Ni, 8 P, and 24 S atoms to model the $NiPS_3$ surface structure (in the case of $NiFePS_3$, the Fe atom substitutes a Ni atom). The $NiPS_3$(100) facet was used as the surface termination. The NiOOH(001) surface was modeled by a twelve-layer slab containing 12 Ni, 24 O, and 12 H atoms. We then constructed a heterostructure model comprising two parts, where the $NiPS_3$(100) and NiOOH(001) combined together in the Z direction. A vacuum layer of 15 Å was used in order to separate the surface slab from its periodic duplicates. To ensure accurate energy calculations, the pristine $NiPS_3$(100) surface was first optimized independently due to the significant rearrangement of $NiPS_3$ atoms during optimization. During the reaction investigations, the optimized $NiPS_3$(100) surface was kept fixed while the other atoms were allowed to relax. and the atomic positions were optimized till the forces were less than 0.02 eV/Å. The structure of isolated molecules (BA, BN, H_2O, and H_2) was optimized within a unit cell measuring 15 Å $\times$ 15 Å $\times$ 15 Å, with only the Γ-point utilized.[64] The effects of van der Waals corrections were modeled using Grimme's method, with Becke–Jonson damping.[64,65]

The binding energy of an adsorbate was calculated as follows:

$$E_{binding} = E_{(slab+adsorbate)} - E_{(slab)} - E_{(adsorbate)}, \quad (4)$$

where $E_{(slab + adsorbate)}$, $E_{(slab)}$, and $E_{(adsorbate)}$ are the total energy of the slab with the adsorbate, the energy of the clean slab, and the energy of the adsorbate in the gas phase, respectively.
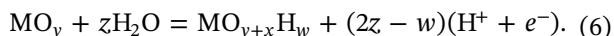
The Gibbs free energy of a species is calculated as follows:

$$G = E + ZPE - TS. \quad (5)$$

Here, E is the total energy of a species obtained from DFT calculations, ZPE and S are the zero-point energy and entropy of a species, respectively, and $T = 298.15$ K.

The theoretical overpotential depends strongly on the coverage of the different reactant species at the surface. We constructed surface Pourbaix diagrams, where we identify the most stable structures for NiOOH(001), $NiOOH/NiFePS_3$, and $NiFeOOH/NiFePS_3$ for a range of potentials at pH = 13.5. Several possible structures have been considered including termination with a single moiety, as well as mixed cases. In our models, there are

three equivalent adsorption sites. Consequently, 3O*, 3OH*, and 3H$_2$O* correspond to the surfaces fully covered by O*, OH*, and H$_2$O*, respectively. Note that other possible adsorption sites exist that may lead to large coverage if multiple site occupancy is allowed, but this will lead to an adsorbate at small distances with concomitant high steric repulsion. Thus, single occupancy has been considered in our models. A surface Pourbaix diagram was constructed by assuming an equilibrium of the surface with water, protons, and electrons according to the following equation:

$$MO_y + zH_2O = MO_{y+x}H_w + (2z - w)(H^+ + e^-). \quad (6)$$

CONFLICT OF INTEREST STATEMENT
The authors declare that there are no conflicts of interests.

ORCID
Ying Yang http://orcid.org/0000-0001-9306-3227
Alberto Vomiero http://orcid.org/0000-0003-2935-1165

REFERENCES
1. Akhade, SA, Singh N, Gutiérrez O, OY, et al. Electrocatalytic hydrogenation of biomass-derived organics: a review. *Chem Rev.* 2020;120(20):11370-11419.
2. Ali T, Wang H, Iqbal W, Bashir T, Shah R, Hu Y. Electrosynthesis of organic compounds with heterogeneous catalysis. *Adv Sci.* 2023;10(1):2205077.
3. Sendeku MG, Shifa TA, Dajan FT, et al. Frontiers in photoelectrochemical catalysis: a focus on valuable product synthesis. *Adv Mater.* 2024;36(21):2308101.
4. Anbarasan P, Schareina T, Beller M. Recent developments and perspectives in palladium-catalyzed cyanation of aryl halides: synthesis of benzonitriles. *Chem Soc Rev.* 2011;40(10):5049-5067.
5. Su F, Mathew SC, Möhlmann L, Antonietti M, Wang X, Blechert S. Aerobic oxidative coupling of amines by carbon nitride photocatalysis with visible light. *Angew Chem Int Ed.* 2011;50(3):657-660.
6. Wang T, Jiao N. Direct approaches to nitriles via highly efficient nitrogenation strategy through C–H or C–C bond cleavage. *Acc Chem Res.* 2014;47(4):1137-1145.
7. Flood TC, Bitler SP. Reversible formal alkene insertion into a chelated platinum-alkyl bond. *J Am Chem Soc.* 1984;106(20):6076-6077.
8. Huang Y, Chong X, Liu C, Liang Y, Zhang B. Boosting hydrogen production by anodic oxidation of primary amines over a NiSe nanorod electrode. *Angew Chem Int Ed.* 2018;57(40):13163-13166.
9. Kim J, Stahl SS. Cu/nitroxyl catalyzed aerobic oxidation of primary amines into nitriles at room temperature. *ACS Catal.* 2013;3(7):1652-1656.
10. Ovoshchnikov DS, Donoeva BG, Golovko VB. Visible-light-driven aerobic oxidation of amines to nitriles over hydrous ruthenium oxide supported on TiO$_2$. *ACS Catal.* 2015;5(1):34-38.
11. Parshad H, Frydenvang K, Liljefors T, Larsen CS. Correlation of aqueous solubility of salts of benzylamine with experimentally and theoretically derived parameters. A multivariate data analysis approach. *Int J Pharm.* 2002;237(1–2):193-207.
12. Ding Y, Miao BQ, Li SN, et al. Benzylamine oxidation boosted electrochemical water-splitting: hydrogen and benzonitrile co-production at ultra-thin Ni$_2$P nanomeshes grown on nickel foam. *Appl Catal B.* 2020;268:118393.
13. Zeng L, Chen W, Zhang Q, et al. CoSe$_2$ subnanometer belts with se vacancies and ni substitutions for the efficient electrosynthesis of high-value-added nitriles coupled with hydrogen generation. *ACS Catal.* 2022;12(18):11391-11401.
14. Sun Y, Shin H, Wang F, et al. Highly selective electrocatalytic oxidation of amines to nitriles assisted by water oxidation on metal-doped α-Ni(OH)$_2$. *J Am Chem Soc.* 2022;144(33):15185-15192.
15. Wen Q, Lin Y, Yang Y, et al. In situ chalcogen leaching manipulates reactant interface toward efficient amine electrooxidation. *ACS Nano.* 2022;16(6):9572-9582.
16. Wang W, Wang Y, Yang R, et al. Vacancy-rich Ni(OH)$_2$ drives the electrooxidation of amino C−N bonds to nitrile C≡N bonds. *Angew Chem Int Ed.* 2020;59(39):16974-16981.
17. Wang Y, Xue Y-Y, Yan L-T, et al. Multimetal incorporation into 2D conductive metal–organic framework nanowires enabling excellent electrocatalytic oxidation of benzylamine to benzonitrile. *ACS Appl Mater Interfaces.* 2020;12(22):24786-24795.
18. Zeng Y, Zhao M, Huang Z, et al. Surface reconstruction of water splitting electrocatalysts. *Adv Energy Mater.* 2022;12(33):2201713.
19. Polo-Garzon F, Bao Z, Zhang X, Huang W, Wu Z. Surface reconstructions of metal oxides and the consequences on catalytic chemistry. *ACS Catal.* 2019;9(6):5692-5707.
20. Duan Y, Sun S, Sun Y, et al. Mastering surface reconstruction of metastable spinel oxides for better water oxidation. *Adv Mater.* 2019;31(12):1807898.
21. Belay Ibrahim, K, Ahmed Shifa, T, Zorzi S, Getaye Sendeku, M, Moretti E Vomiero A. Emerging 2D materials beyond mxenes and TMDs: transition metal carbo-chalcogenides. *Prog Mater Sci.* 2024;144:101287.
22. He Z, Ajmal M, Zhang M, et al. Progress in manipulating dynamic surface reconstruction via anion modulation for electrocatalytic water oxidation. *Adv Sci.* 2023;10(29):2304071.

23. Sun Y, Wang J, Xi S, et al. Navigating surface reconstruction of spinel oxides for electrochemical water oxidation. *Nat Commun.* 2023;14(1):2467.

24. Bender MT, Choi K-S. Electrochemical dehydrogenation pathways of amines to nitriles on NiOOH. *JACS Au.* 2022;2(5):1169-1180.

25. Samal R, Sanyal G, Chakraborty B, Rout CS. Two-dimensional transition metal phosphorous trichalcogenides (MPX$_3$): a review on emerging trends, current state and future perspectives. *J Mater Chem A.* 2021;9(5):2560-2591.

26. Sendeku MG, Harrath K, Dajan FT, et al. Deciphering in-situ surface reconstruction in two-dimensional CdPS$_3$ nanosheets for efficient biomass hydrogenation. *Nat Commun.* 2024;15(1):5174.

27. Gusmão R, Sofer Z, Sedmidubský D, Huber Š, Pumera M. The role of the metal element in layered metal phosphorus triselenides upon their electrochemical sensing and energy applications. *ACS Catal.* 2017;7(12):8159-8170.

28. Mukherjee D, Austeria PM, Sampath S. Two-dimensional, few-layer phosphochalcogenide, FePS$_3$: a new catalyst for electrochemical hydrogen evolution over wide pH range. *ACS Energy Lett.* 2016;1(2):367-372.

29. Hao Y, Huang A, Han S, et al. Plasma-treated ultrathin ternary FePSe$_3$ nanosheets as a bifunctional electrocatalyst for efficient zinc–air batteries. *ACS Appl Mater Interfaces.* 2020;12(26):29393-29403.

30. Mayorga-Martinez CC, Sofer Z, Sedmidubský D, Huber Š, Eng AYS, Pumera M. Layered metal thiophosphite materials: magnetic, electrochemical, and electronic properties. *ACS Appl Mater Interfaces.* 2017;9(14):12563-12573.

31. Wu B, Zhan X, Yu P, et al. Photocatalytic co-production of hydrogen gas and N-benzylidenebenzylamine over high-quality 2D layered In$_{4/3}$P$_2$Se$_6$ nanosheets. *Nanoscale.* 2022;14(41):15442-15450.

32. Song B, Li K, Yin Y, et al. Tuning mixed nickel iron phosphosulfide nanosheet electrocatalysts for enhanced hydrogen and oxygen evolution. *ACS Catal.* 2017;7(12):8549-8557.

33. Dong B, Li W, Huang X, et al. Fabrication of hierarchical hollow Mn doped Ni(OH)$_2$ nanostructures with enhanced catalytic activity towards electrochemical oxidation of methanol. *Nano Energy.* 2019;55:37-41.

34. Zhao B, Liu J, Xu C, et al. Hollow NiSe nanocrystals heterogenized with carbon nanotubes for efficient electrocatalytic methanol upgrading to boost hydrogen co-production. *Adv Funct Mater.* 2021;31(8):2008812.

35. Wang J, Gao Y, Kong H, et al. Non-precious-metal catalysts for alkaline water electrolysis: operando characterizations, theoretical calculations, and recent advances. *Chem Soc Rev.* 2020;49(24):9154-9196.

36. Zheng X, Zhang B, De LunaLuna, P, et al. Theory-driven design of high-valence metal sites for water oxidation confirmed using in situ soft X-ray absorption. *Nat Chem.* 2018;10(2):149-154.

37. Wang F, Shifa TA, He P, et al. Two-dimensional metal phosphorus trisulfide nanosheet with solar hydrogen-evolving activity. *Nano Energy.* 2017;40:673-680.

38. Xue Y, Liu M, Qin Y, et al. Ultrathin NiFeS nanosheets as highly active electrocatalysts for oxygen evolution reaction. *Chin Chem Lett.* 2022;33(8):3916-3920.

39. Cheng Z, Shifa TA, Wang F, et al. High-yield production of monolayer FePS$_3$ quantum sheets via chemical exfoliation for efficient photocatalytic hydrogen evolution. *Adv Mater.* 2018;30(26):1707433.

40. Konkena B, Masa J, Botz AJR, et al. Metallic NiPS$_3$@NiOOH core–shell heterostructures as highly efficient and stable electrocatalyst for the oxygen evolution reaction. *ACS Catal.* 2017;7(1):229-237.

41. Xue S, Chen L, Liu Z, Cheng H-M, Ren W. NiPS$_3$ nanosheet–graphene composites as highly efficient electrocatalysts for oxygen evolution reaction. *ACS Nano.* 2018;12(6):5297-5305.

42. Ge R, Wang Y, Li Z, et al. Selective electrooxidation of biomass-derived alcohols to aldehydes in a neutral medium: promoted water dissociation over a nickel-oxide-supported ruthenium single-atom catalyst. *Angew Chem Int Ed.* 2022;61(19):e202200211.

43. Mondal I, Hausmann JN, Vijaykumar G, et al. Nanostructured intermetallic nickel silicide (pre)catalyst for anodic oxygen evolution reaction and selective dehydrogenation of primary amines. *Adv Energy Mater.* 2022;12(25):2200269.

44. Liu D, Liu J-C, Cai W, et al. Selective photoelectrochemical oxidation of glycerol to high value-added dihydroxyacetone. *Nat Commun.* 2019;10(1):1779.

45. Du J, You S, Li X, et al. In situ crystallization of active NiOOH/CoOOH heterostructures with hydroxide ion adsorption sites on velutipes-like CoSe/NiSe nanorods as catalysts for oxygen evolution and cocatalysts for methanol oxidation. *ACS Appl Mater Interfaces.* 2019;12(1):686-697.

46. Gallenberger J, Moreno Fernández H, Alkemper A, et al. Stability and decomposition pathways of the NiOOH OER active phase of NiO$_x$ electrocatalysts at open circuit potential traced by ex situ and in situ spectroscopies. *Catal Sci Technol.* 2023;13(16):4693-4700.

47. Ibrahim KB, Shifa TA, Moras P, Moretti E, Vomiero A. Facile electron transfer in atomically coupled heterointerface for accelerated oxygen evolution. *Small.* 2023;19(1):2204765.

48. Solomon G, Landström A, Mazzaro R, et al. NiMoO$_4$@Co$_3$O$_4$ core–shell nanorods: in situ catalyst reconstruction toward high efficiency oxygen evolution reaction. *Adv Energy Mater.* 2021;11(32):2101324.

49. Ge X, Chen Y, Liu S, Yang X, Feng, X, Feng K. NaV (SO$_4$)$_2$/C, Na$_3$V(SO$_4$)$_3$/C, and K$_2$VO (SO$_4$)$_2$/C: three Li-free vanadium sulfate cathode materials for lithium-ion batteries. *J Solid State Electrochem.* 2022;26(8):1627-1636.

50. Wu B, Gong S, Lin Y, et al. A unique NiOOH@FeOOH heteroarchitecture for enhanced oxygen evolution in saline water. *Adv Mater.* 2022;34(43):2108619.

51. Li Y, Jiao Y, Yan H, et al. Mo−Ni-based heterojunction with fine-customized d-band centers for hydrogen production coupled with benzylamine electrooxidation in low alkaline medium. *Angew Chem Int Ed.* 2023;62(39):e202306640.

52. Ibrahim KB, Shifa TA, Bordin M, Moretti E, Wu H-L, Vomiero A. Confinement accelerates water oxidation catalysis: evidence from in situ studies. *Small Methods.* 2023;7(10):2300348.

53. Hausmann JN, Menezes PW. Effect of surface-adsorbed and intercalated (oxy)anions on the oxygen evolution reaction. *Angew Chem Int Ed.* 2022;61(38):e202207279.

54. Xiao W, Zhang L, Bukhvalov D, et al. Hierarchical ultrathin carbon encapsulating transition metal doped MoP electrocatalysts for

efficient and pH-universal hydrogen evolution reaction. *Nano Energy*. 2020;70:104445.

55. Xiao W, Yan D, Zhang Y, Yang X, Zhang T. Heterostructured $MoSe_2$/oxygen-terminated Ti_3C_2 MXene architectures for efficient electrocatalytic hydrogen evolution. *Energy Fuels*. 2021;35(5):4609-4615.

56. Liu K, Wang F, He P, et al. The role of active oxide species for electrochemical water oxidation on the surface of 3d-Metal phosphides. *Adv Energy Mater*. 2018;8(15):1703290.

57. Song YZ, Zhang W, Chen J, et al. Synthesis of FeS nanoparticles for the catalytic reduction of 2,4-dinitrochlorobenzene. *Russ J Phys Chem A*. 2020;94(6):1184-1189.

58. Li X, Hu Y, Dong F, et al. Non-noble-metallic Ni_2P nanoparticles modified O_v-BiOBr with boosting photoelectrochemical hydrogen evolution without sacrificial agent. *Appl Catal B*. 2023;325:122341.

59. Perdew JP, Burke K, Ernzerhof M. Generalized gradient approximation made simple. *Phys Rev Lett*. 1996;77(18): 3865-3868.

60. Version vasp.5.3.5. November, 2023. http://www.vasp.at

61. Kresse G, Joubert D. From ultrasoft pseudopotentials to the projector augmented-wave method. *Phys Rev B*. 1999;59(3): 1758-1775.

62. Blöchl PE. Projector augmented-wave method. *Phys Rev B*. 1994;50(24):17953-17979.

63. Bahri L, Mbarki F, Harrath K. Understanding the direct methane conversion to oxygenates on graphene-supported single 3d metal atom catalysts. *Chem Pap*. 2023;77(7):3759-3767.

64. Grimme S. Density functional theory with London dispersion corrections. *WIREs Comput Mol Sci*. 2011;1(2):211-228.

65. Grimme S, Antony J, Ehrlich S Krieg H A consistent and accurate ab initio parametrization of density functional dispersion correction (DFT-D) for the 94 elements H-Pu. *J Chem Phys* 2010; 132 (15); 154104.

SUPPORTING INFORMATION

Additional supporting information can be found online in the Supporting Information section at the end of this article.